Research Article Vol. 33, No. 24 / 1 Dec 2025 / Optics Express 51417
Optics EXPRESS

Predictive adaptive optics optimal control for LEO communications in low elevation and strong scintillation conditions

JOANA SUL TORRES,[1,2,*] HENRI-FRANÇOIS RAYNAUD,[2] ILIJA R. HRISTOVSKI,[1] GIANLUCA LA TORRE,[1] DOUGLAS LAIDLAW,[1] ANDREW PAUL REEVES,[3] AND CAROLINE KULCSÁR[2]

[1]*Institute of Communications and Navigation, German Aerospace Centre (DLR), 82234 Weßling, Germany*
[2]*Université Paris-Saclay, Institut d'Optique Graduate School, CNRS, Laboratoire Charles Fabry, 91127, Palaiseau, France*
[3]*Space Research Centre, Physics Department, Durham University, South Road, Durham, DH1 3LE, UK*
[*]*joana.dosuldamotatorres@dlr.de*

Abstract: Free space optical communication (FSOC) links have significant advantages over conventional radio frequency transmissions. However, optical light travelling through atmospheric turbulence is subject to varying diffraction rates that distort the wavefront phase, impacting the performance of optical links. Adaptive optics (AO) systems have been shown to mitigate these effects. An integral action controller is typically used in FSOC AO systems. The performance of these controllers is limited by the time delay. In addition, the intensity fluctuations due to scintillation can render the AO loop unstable. As a result, integrators do not perform well in strong turbulence conditions. Predictive control algorithms have the potential to improve coupling efficiency. This simulation-based study concentrates on demonstrating and quantifying the effectiveness of zonal-based linear quadratic Gaussian (LQG) regulators for LEO downlinks at low elevation and high scintillation scenarios, based on the works in Prengère et al. [J. Opt. Soc. Am. A **37**, 1083 (2020)] related to satellite tracking. The simulation includes Fresnel propagation, an aspect typically neglected in existing studies. A phase oversampling and edge compensation model changes are considered as potential LQG improvements. Results are compared to a tuned integrator, and it is shown that the best performing zonal-based LQG improves mean coupling efficiency by 70%.

1. Introduction

Earth-to-satellite communications typically use radio transmission wavelengths at which the atmosphere is transparent. However, the radio spectrum is saturated and unable to address modern day connectivity demands [1]. Free Space Optical Communication (FSOC) is an emerging technology that aims to perform these transmissions at optical to Near-Infrared (NIR) wavelengths. Advantages over radio include higher bandwidths (of the order of Tb/s), smaller beam divergence and the potential to support quantum encryption. Such advantages allow FSOC to address ever growing demands for higher data rates and global connectivity [1,2]. Global network solutions built on FSOC feederlinks are currently under development, making it a prolific research field [2,3]. However advantageous, optical wavelengths are perturbed by atmospheric turbulence, leading to aberrations in the propagated wavefront [4,5]. To support modern, high bandwidth terrestrial photonics communications components, the light received by an Optical Ground Station (OGS) should be coupled into a Single Mode Fibre (SMF). However wavefront distortions

#574467 https://doi.org/10.1364/OE.574467
Journal © 2025 Received 25 Jul 2025; revised 7 Nov 2025; accepted 7 Nov 2025; published 26 Nov 2025

Optics EXPRESS

cause quickly changing speckles in the telescope focal plane, resulting in low and quickly varying coupling efficiency.

Adaptive optics (AO) systems have been demonstrated to help correct these effects and improve the FSOC link performance by enhancing the coupling of light into an SMF and reducing the overall fade count and time [6]. However, the strong scintillation observed at the OGS telescope aperture in FSOC links can lead to missing measurements on the wavefront sensor. In these conditions, classical integrator control leads to elevated fade count which translates into significant loss of data and link deterioration [7–9]. In addition, LEO and MEO satellites must be tracked across the sky, increasing the apparent wind speed of the turbulence, thus increasing the rate at which the wavefront changes. These effects aggravate at lower elevations, especially when considering stronger daylight turbulence conditions across the line of sight.

Predictive AO control algorithms have the potential to bring performance improvements to FSOC feederlinks [8,10]. Prengère et al. [10] obtained ≈ 50% Strehl ratio with a zonal-based LQG regulator (against ≈ 10% for the standard integrator) for simulations of LEO satellite tracking; Robles et al. [11] shows that a modal-based LQG approach for LEO downlinks can achieve similar coupling performance as an integrator at double the frequency. Both studies demonstrate high potential gains in fibre coupling performance through the use of an LQG regulator tested through Monte-Carlo AO simulations. However, these studies simulate only geometric light propagation, which is not well suited to the stronger turbulence conditions that are experienced during FSOC links. In particular, the absence of diffraction calculations excludes scintillation effects, where even small phase disturbances lead to rapidly changing focus and defocus of light on the ground. Given the requirement for FSOC links to operate in the most challenging conditions, these effects need to be accounted for. The validity of these regulators considering diffractive effects at low elevations is yet to be investigated. To the best of the authors' knowledge, there are no reported end-to-end simulation results for predictive regulators considering angular spectrum propagation on a LEO downlink.

The aim of this article is to explore and optimise the performance of predictive LQG AO regulators, proposed in [10] for satellite tracking with geometric propagation, for FSOC scenarios. We particularly consider the adverse turbulence conditions experienced during LEO-to-ground links at low elevations. In order to do so, scintillation effects are included in the atmospheric light propagation models and their impact is demonstrated. A zonal-based (i.e. wavefront as phase values defined directly on a discrete sampling grid) LQG approach to AO control, following the works in [10], is considered and performance is compared to that of an integrator under realistic worst-case scenario LEO downlink conditions. Phase oversampling is implemented to create a higher fidelity controller model that accounts more accurately for turbulence translation across the telescope and measurement process. In addition, edge compensation [10] is also considered, where an additional ring of phase points outside the pupil is included in the predictive model. Each resulting regulator is subject to performance comparisons with a tuned integrator in terms of resulting coupling loss and fade statistics.

2. FSOC-AO propagation simulator configuration

For this research work, an end-to-end Monte Carlo simulator is used. This simulator is a modular Python based solution developed in-house at DLR (German Aerospace Centre) with the purpose of modelling light propagation and AO compensation for FSOC. This simulator has been tested against various theoretical results and shows good agreement with modeled FSOC links [12]. A visual summary of the simulated system is described in Fig. 1.

Light is assumed to enter the atmosphere as a plane wave, as the satellite is far from the top of the atmosphere relative to the beam size. It is propagated between atmospheric layers using either a geometric or physical propagation algorithm (e.g., angular spectrum). An aperture function is applied to the electric field distribution at the ground, and the result corrected by a simulated

Optics EXPRESS

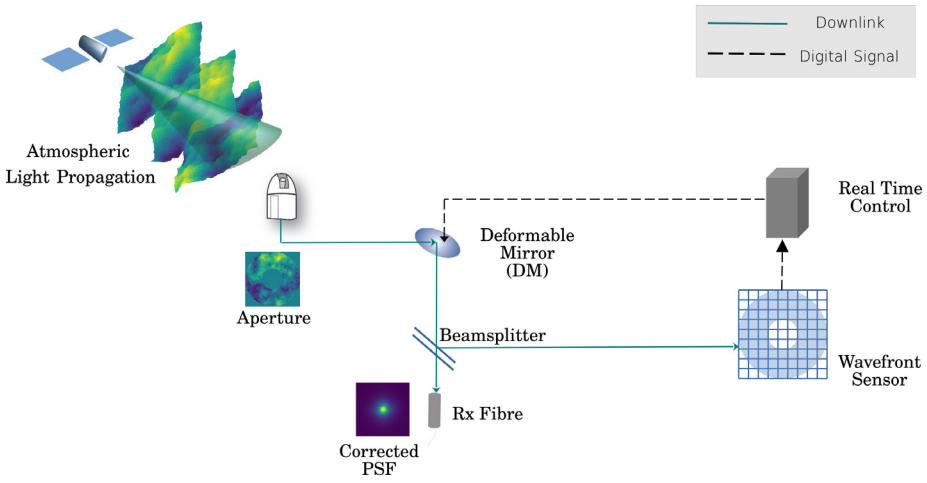

Fig. 1. Visualisation of the simulation configuration. Light from a point source is propagated along the line of sight, and the resulting wavefront is masked according to the telescope aperture.

deformable mirror (DM). The residual electric field is observed by a simulated Shack-Hartmann Wavefront Sensor (WFS), using a full diffractive model and therefore including scintillation effects on sub-apertures. DM commands are computed from WFS using various prototype AO controllers. A delay of 2 frames is assumed between wavefront sensing and DM settling into commanded shape. The residual electric field is also simulated to be coupled into a single mode fibre (SMF) by performing an overlap integral with the SMF mode.

2.1. Simulated turbulence conditions

Atmospheric turbulence was modeled using the Hufnagel–Valley 5/7 profile [13], with turbulence strength at altitude h calculated as:

$$C_n^2(h) = 0.00594\left(\frac{W}{27}\right)^2 (10^{-5}h)^{10} e^{-h/1000} + 2.7\times 10^{-16} e^{-h/1500} + A\, e^{-h/100}, \tag{1}$$

where A is the ground-level turbulence coefficient and W is the RMS wind speed at high altitudes. These are empirical values, and here taken to be 1×10^{-13} m$^{-2/3}$ and 114.8 m/s respectively, corresponding to the strong turbulence case for LEO satellite links at daytime reported in [14]. This approach aims to ensure a realistic estimate of atmospheric dynamics encountered during typical LEO passes at 1000 km altitude. The profile was then discretized according to the equivalent layer method [15], so that the integrated parameters are preserved. Wind profiles were calculated for three different elevations according to the Greenwood model [16]:

$$V(h) = V_g + V_T \exp\left[-\left(\frac{h\cos(\zeta) - H_T}{L_T}\right)^2\right] \times \left[\sin^2\varphi + \cos^2\varphi\cos^2\zeta\right]^{1/2}, \tag{2}$$

where V_g and V_T are respectively the ground and tropopause wind speeds; ζ is the zenith angle; H_T and L_T are height and thickness of the tropopause layer, and φ is the wind direction relative to the telescope azimuth. The resulting discretized turbulence profiles for each elevation angle considered are summarised in Table 1. The turbulence profile is presented at zenith, but internally integrated to the correct elevation for each SimID.

Optics EXPRESS

Table 1. Summary of the simulated turbulence conditions by atmospheric layer. The wind profiles consider the apparent wind dependence on satellite elevation to be a dominant effect, and thus all layers are assumed to have the same direction.

Altitude (m)	Cn^2dh Profile ($m^{-1/3}$)	SimID 80° (m/s)	SimID 50° (m/s)	SimID 30° (m/s)
242	1.03×10^{-11}	8.08	8.04	7.99
6036	5.20×10^{-14}	68.01	61.39	55.21
9093	6.96×10^{-14}	100.75	95.18	83.17
12325	5.67×10^{-14}	117.06	124.93	114.77
15709	2.10×10^{-14}	126.89	142.32	147.16
19168	4.63×10^{-15}	146.24	154.69	175.13
22664	7.25×10^{-16}	170.95	173.00	196.25

The transverse wind speed in each turbulent layer is projected along the slant path of the optical beam, causing the effective wind speed seen by the optical beam to increase as the elevation angle decreases. Table 2 summarises the atmospheric parameters for each of the simulation scenarios. The parameters were computed both at the seeing wavelength of 155 nm and usual standard of 500 nm for ease of comparison.

Table 2. Summary of atmospheric parameters for the different SimIDs, at both the standard wavelength of 500 nm for ease of comparison and the actual seeing wavelength of 1550 nm.

Atmospheric Parameters	τ_0 (ms)		θ_0 (μ rad)		r_0 (cm)		σ_R^2	
Wavelength (nm)	**500**	**1550**	**500**	**1550**	**500**	**1550**	**500**	**1550**
SimID30°	0.3	1.2	1.91	7.42	1.08	4.19	2.22	0.59
SimID50°	0.4	1.5	3.78	14.67	1.39	5.41	1.01	0.27
SimID80°	0.5	1.7	5.64	21.93	1.94	7.54	0.64	0.17

In Table 2, the parameters suggest a stronger turbulence than in astronomical cases. In particular, the Rytov variance σ_R^2 values suggest strong scintillation conditions consistent with those reported on-sky in [17].

In order to evaluate how including diffraction can affect FSOC simulation results and the conclusions drawn, two optical propagation methods were compared. With the geometric propagation method, the phase at each layer is computed per time step and is summed element-wise to determine the integrated phase change on the propagated beam of light. For the physical propagation, the angular spectrum propagation method (ASP) described by Schmidt in [18] was used.

As is evident in Fig. 2, diffraction causes significant intensity fluctuations on the detector. As scintillation on the WFS increases, the performance has been shown to degrade and this has been correlated with the presence in the phase of so called branch points [9,19]. This results in degraded or even missing measurements, an effect noticeable in Fig. 2(b). These phenomena have the potential to destabilize the AO loop when using a classical integrator.

2.2. AO integrator

The most commonly deployed AO regulator is the integrator. The command vector u_k to be applied at physical time kT_s, where T_s is the sampling period, is computed as

$$u_k = u_{k-1} + gM_{\text{com}}y_k, \tag{3}$$

Optics EXPRESS

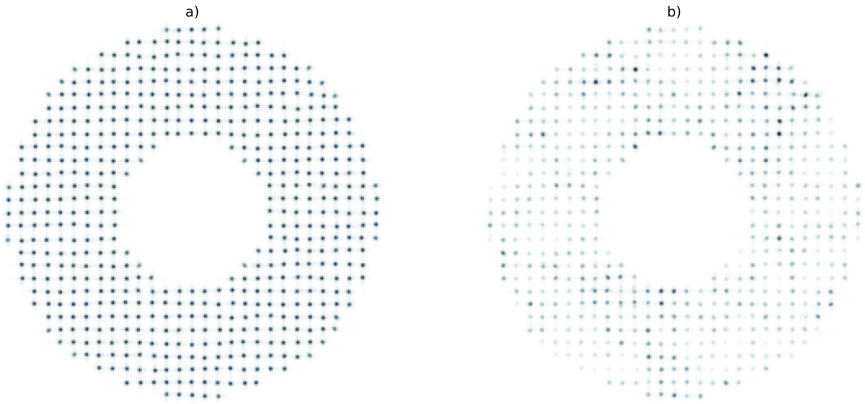

Fig. 2. Comparison of the same frame as seen on the WFS: a) considering solely geometric propagation of light (no scintillation); b) considering the physical propagation method with angular spectrum propagation (with scintillation). Intensity fluctuations are visible, with most subapertures collecting significantly less light in b) than a).

where g is the integrator gain and y is the measurement vector. The command matrix M_{com} is the pseudo-inverse of the interaction matrix M_{int} mapping DM commands onto WFS measurements. This matrix is easily obtained during AO calibration. The integrator has been extensively used and characterized in scientific literature in the context of AO. In this work, it serves as a benchmark to the proposed alternative control method.

3. Optimal predictive AO control and state-space modelling

LQG regulators are optimal controllers designed by minimizing a quadratic cost function. For AO systems that can be accurately represented by a linear state model driven by Gaussian white noises, LQG control has been shown to minimize the variance of the residual phase ϕ^{res} [20–22]. This residual phase is the difference between the incoming phase ϕ and the correction phase ϕ^{cor} generated by the DM, that is, $\phi^{\text{res}} = \phi - \phi^{\text{cor}}$. When ϕ is a stationary vector-valued stochastic process, the optimal control u_k minimizes the performance criterion

$$J_k^{\text{d}}(u_k) \triangleq \text{E}\left(||\phi_k^{\text{res}}||^2 \mid \Im_k\right) \triangleq \text{trace}\left(\text{Var}\left(\phi_k^{\text{res}} \mid \Im_k\right)\right), \tag{4}$$

where $\Im_k$ represents all the information available at time index k. (Here and throughout this paper, x_k will denote the average of the continuous-time variable $x(t)$ over the sampling interval $(k-1)T_s \leq t < kT_s$.)

We consider here the standard case of a 2-frame-delay system, 1 frame for WFS integration and 1 frame for camera read-out and all calculations and data transfers. When the DM's response is fast enough with respect to T_s, so that the correction phase can be written from the DM influence functions matrix N as $\phi_k^{\text{cor}} = Nu_{k-1}$, the optimal control is given by

$$u_k \triangleq \arg\min_{u_k}\left(J_k^{\text{d}}(u_k)\right) = (N^{\text{T}}N)^{-1}N^{\text{T}}\widehat{\phi}_{k+1|k}, \tag{5}$$

where the conditional expectation $\widehat{\phi}_{k+1|k} = \text{E}(\phi_{k+1} \mid \Im_k)$ is the minimum-variance one-step-ahead prediction of ϕ_k knowing all past information up to time k. The optimal prediction problem is shown to be solved constructively using a Kalman filter based on a linear stochastic state space

Optics EXPRESS

model of the incoming disturbance and WFS measurement. The reader may refer to [22] for more detailed developments about this optimal control calculation.

We briefly recall here the construction of the optimal prediction. First, the disturbance and measurement models are combined into a single state-space model in the form:

$$\begin{cases} X_{k+1} = AX_k + \Gamma v_k \\ \phi_k = C_1 X_k \\ y_k = CX_k + w_k + M_{\text{int}} u_{k-2}, \end{cases} \tag{6}$$

where A, Γ and C_1 define a chosen disturbance model (described in section 3.1), and C the WFS measurement model, while v and w are mutually independent zero-mean vector-valued Gaussian white noises, with covariance matrices Σ_v and Σ_w. The interaction matrix M_{int} can be expressed as a function of the WFS matrix D and the influence functions matrix N as $M_{\text{int}} = DN$. The optimal disturbance prediction is then obtained as $\widehat{\phi}_{k+1|k} = C_1 \widehat{X}_{k+1|k}$, where $\widehat{X}_{k+1|k}$ is computed in real time as:

$$\widehat{X}_{k+1|k} = (\mathrm{A} - L_\infty C)\, \widehat{X}_{k|k-1} + L_\infty \left(y_k - M_{\text{int}} u_{k-2}\right) . \tag{7}$$

In this recursive equation, L_∞ is the asymptotic Kalman gain, which is given by:

$$L_\infty = A\Sigma_\infty C^{\mathrm{T}} (C\Sigma_\infty C^{\mathrm{T}} + \gamma \Sigma_w)^{-1}, \tag{8}$$

where Σ_∞ is the asymptotic prediction error covariance and γ is the so-called fudge factor allowing for tuning of the asymptotic filter. The fudge factor is used to globally affect the noise variance. Modifying the measurement noise variance in the Kalman filter is commonly used to absorb model discrepancies, see, e.g. [23,24] for its use in AO. The matrix Σ_∞ is computed as the unique solution of the Discrete Algebraic Riccati Equation that writes

$$\Sigma_\infty = A\Sigma_\infty A^{\mathrm{T}} + \Gamma \Sigma_v \Gamma^{\mathrm{T}} - A\Sigma_\infty C^{\mathrm{T}} (C\Sigma_\infty C^{\mathrm{T}} + \gamma \Sigma_w)^{-1} C\Sigma_\infty A^{\mathrm{T}} . \tag{9}$$

3.1. Disturbance modeling and priors

Several methods can be chosen to obtain an adequate model of the incoming wavefront, ranging from purely theoretical [20] to entirely data-driven and data-based [24]. Also, the wavefront ϕ can be represented in a basis of optical modes (usually Zernike of Karhunen-Loève modes) or on a zonal basis, that is, sampled over a regular grid of phase points taken over the telescope pupil. In this paper, following [10], we use a zonal representation in which the incoming wavefront model is derived from theoretical spatial and temporal correlations. These are computed from turbulence and wind priors with the von Kármán phase structure function and following the frozen-flow Taylor hypothesis. According to these priors, atmospheric turbulence is spatially discretized in altitude as a finite number of thin layers, each of which exhibits von Kármán spatial statistics and is moving with constant speed and direction [25]. We briefly recall here the essential features of the zonal approach in [10]. First, the variance-covariance matrix $\Sigma_\phi = \mathrm{Var}(\phi_k)$ of the phase points in the telescope's pupil is computed from the von Kármán phase structure function. Combining the von Kármán phase structure function and the frozen-flow assumption also enables to compute the temporal cross-covariance matrices $C_\phi(1) = \mathrm{Cov}(\phi_{k+1}, \phi_k)$ and $C_\phi(2) = \mathrm{Cov}(\phi_{k+2}, \phi_k)$. The next step is to match these spatio-temporal statistics to a vector-valued auto-regressive stochastic model of order 2 in the form:

$$\phi_{k+1} = A_1 \phi_k + A_2 \phi_{k-1} + v_k . \tag{10}$$

The parameters of this model are the matrices A_1, A_2 and Σ_v. Matching the values of $C_\phi(1)$, $C_\phi(2)$ computed from this AR(2) model with the values given by the frozen-flow model amounts

Optics EXPRESS

to solving the so-called Yule-Walker equations in the unknowns A_1, A_2 and Σ_v. To achieve this, the AR(2) model is put in the standard state-space form:

$$X_{k+1} = AX_k + \Gamma v_k = \begin{pmatrix} A_1 & A_2 \\ I & 0 \end{pmatrix} X_k + \begin{pmatrix} I \\ 0 \end{pmatrix} v_k, \; X_k = \begin{pmatrix} \phi_k \\ \phi_{k-1} \end{pmatrix} \tag{11}$$
$$\phi_k = C_1 X_k = \begin{pmatrix} I & 0 \end{pmatrix} X_k \, .$$

In the steady-state regime, the covariance matrix of X_k should then be equal to

$$\Sigma_X = \begin{pmatrix} \Sigma_\phi & C_\phi(1)^{\mathrm{T}} \\ C_\phi(1) & \Sigma_\phi \end{pmatrix}. \tag{12}$$

The values of A_1, A_2 are then given by

$$\begin{pmatrix} A_1 & A_2 \end{pmatrix} = \begin{pmatrix} C_\phi(1) & C_\phi(2) \end{pmatrix} \Sigma_X^{-1} \, . \tag{13}$$

Finally, the value of the noise covariance Σ_v is deduced from the identity $\Gamma\Sigma_v\Gamma^{\mathrm{T}} = \Sigma_X - A\Sigma_X A^{\mathrm{T}}$. These equations can be used whatever the phase basis. They have been proposed in classical AO for satellite applications in [10] with a zonal basis, they have been used for similar applications in a Zernike basis [11] and could also be considered with, e.g., a Karhunen-Loève basis. In this case, because there is no analytical expression of the phase covariance, variance and covariance matrices will need to be computed numerically from the structure function.

3.2. *Oversampling and edge mitigation*

The FSOC AO system considered in this paper follows a standard so-called Fried geometry, where the actuators are positioned at the corner of the WFS subapertures, so that actuators pitch is equal to subapertures width. The telescope features a central obscuration (which in our case is fairly large, about one-third of the pupil diameter). The baseline choice for zonal AO control is to sample the wavefronts at the same spatial resolution, with phase points at each actuators location including the central obscuration. However, it has been shown that oversampling the phase by a linear factor of two (that is, taking four phase points per WFS subaperture) could significantly improve AO performance [10], together with an extension of the zonal grid beyond the pupil's edges. In the simulations presented in this paper, both approaches were used. This extension is illustrated in Fig. 3. Extending the prediction grid allows the Kalman filter to account for correlations between partially observed regions and improves prediction quality in the absence or deterioration of data near the obscured zone. Incorporating both edge and obscuration effects ensures consistent support for the spatio-temporal structure of the disturbance, which is critical for accurate phase estimation.

4. End-to-end simulation for LQG performance assessment

In order to assess which modification brings the most benefit, three LQG architectures in total are synthesized and simulated, with features summarized in Table 3. These are evaluated at three elevation angles (30°, 50°, and 80°), corresponding to the turbulence conditions described in Table 1. In each presented analysis, the regulators are compared to a tuned integrator as a benchmark. The LQG regulators are using the optimal priors in each case, unless explicitly stated otherwise. Moreover, as explained above, the LQG regulators are further tuned via the fudge factor γ which modifies the signal-to-noise ratio used by the Kalman filter. This allows to recover a performance level very close to optimality but also good robustness margins despite some model mismatch and nonlinearities.

Optics EXPRESS

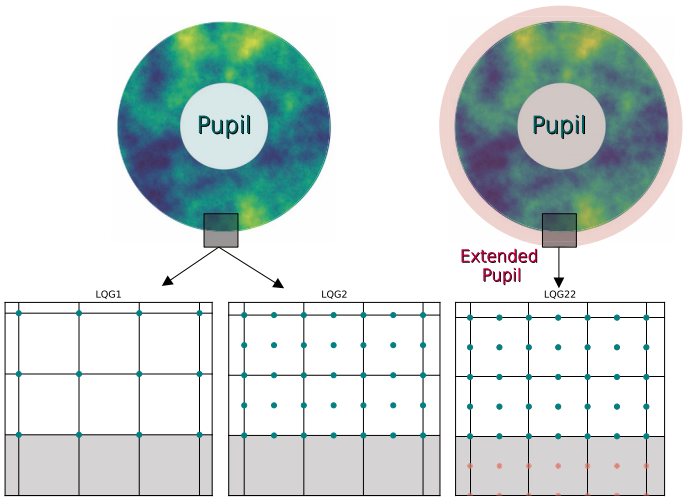

Fig. 3. Zoom in of the phase sampling grid for each regulator superimposed to the WFS grid. White squares represent active WFS subapertures, whilst gray ones are outside the pupil and unilluminated. LQG1 phase sampling grid corresponds to the actuator grid in a Fried configuration; LQG2 oversamples phase points by a factor of 2 in each direction; LQG22 oversamples and extends phase points to an extra ring of subapertures outside the pupil.

Table 3. Summary of regulators tested in the SimID 30° scenario, comprising a mix of simplified grid, oversampling, and edge extension in number of subapertures. Central obscuration is included for all regulators.

Regulator	Oversampling	Edge	Total grid points
LQG1	1×	0	720
LQG2	2×	0	2889
LQG22	2×	2	3269

Table 4 summarizes the optical and hardware configuration and the simulation methodology used across presented results. The parameters match those of the OGS-OP AO system at DLR.

4.1. LQG regulators performance assessment over SimID 30° Scenario

In order to assess the LQG regulator with most suitable architecture, SimID 30° was chosen as it represents the worst elevation case in consideration within the scope of this study. The tuned LQG controllers are evaluated against a tuned integrator as a performance benchmark. The performance of all regulators simulated for this scenario is summarised in Fig. 4 for coupling loss comparisons and Table 5 for fade statistics analysis.

Overall, it is clear the LQG regulators ensure best performance when compared to a tuned integrator. The normalized distribution as well as the cumulative probability functions (Fig. 4) show a clear visual distinction between integrator and LQG regulators, and more notably between LQG1 and LQG2/22. Moreover, an oversampled model for the LQG (LQG2) brings a mean improvement of 1.38±0.02 dB over the non-oversampled LQG1, and a reduction of 85% on the −3 dB fade events quantified in Table 5. LQG22, implementing both the oversampling and edge mitigation techniques, shows a marginal improvement over the LQG2 when it comes to mean and

Optics EXPRESS

Table 4. AO system parameters used in the end-to-end simulations. The physical AO system parameters match those of the Optical Ground Station of Oberpfaffenhofen (OGS-OP) at the Institute for Communication and Navigation (KN-DLR).

Parameter	Value
Telescope aperture	0.8 m
Central obscuration	0.3 m
DM	32x32 grid, 812 valid actuators
Shack-Hartmann WFS	29x29 subapertures, 1088 total measurements, 8x8 pixels per subaperture
Rx Wavelength	1550 nm
AO loop rate $F_s = \frac{1}{T_s}$	2 kHz
Delay	2 frames (1 ms)
Run duration	5 s (10,000 iterations with first 50 discarded in analysis)
Runs per case	3, different random seeds
Total duration	15 s per case

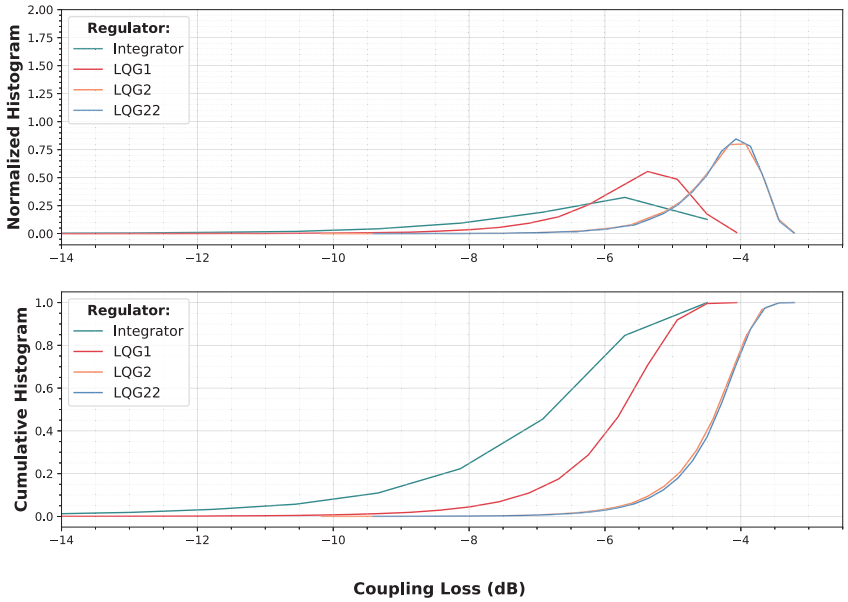

Fig. 4. Normalized histogram (top) and cumulative histogram (bottom) comparison between the integrator and the different simulated LQG regulators for SimID30°. Each regulator was tuned to their best performance for the considered SimID case. The color codes correspond to the regulator types: integrator (green), LQG1 (red), LQG2 (orange), and LQG22 (blue). The x-axis represents the coupling loss in decibel (dB), while the y-axes show the normalized distribution and cumulative probability of the coupling loss, respectively.

Optics EXPRESS

Table 5. Performance summary for SimID30° for all simulated regulators, resulting standard error of the mean SE±0.01 dB. Coupling loss mean and median, as well as fade statistics at thresholds of −3 dB, −6 dB, and −10 dB with fade count per second (F/s) and mean fade duration (ms).

SimID30°	Coupling Loss (dB)		−3 dB		−6 dB		−10 dB	
	Mean	Med.	F/s	ms	F/s	ms	F/s	ms
Integrator	−6.65	−6.15	42	1.86	15	1.33	4	1.08
LQG1	−5.75	−5.52	20	0.95	2	0.78	<1	0.50
LQG2	−4.37	−4.23	3	1.12	0	–	0	–
LQG22	−4.35	−4.21	3	1.02	0	–	0	–

median coupling loss, and although the fade count is not improved, the fade duration is lowered by 0.1 ms.

4.2. *LQG22 performance with SimID50° and SimID80°*

Tables 6 and 7 together with Fig. 5 show that LQG22 consistently outperforms the integrator in both coupling efficiency and fading statistics. The improvement in median coupling loss is within 31-33%. The curves on Fig. 5 represent the empirical coupling loss distributions (histogram, top) and the corresponding cumulative probabilities (bottom). As expected, the distributions flatten with decreased elevation. The cumulative probabilities plots show that in terms of total coupling loss, LQG22 in its worst conditions (SimID30°) outperforms the integrator at its best simulated condition (SimID80°). As is also notable from the normalized histogram and cumulative probability plots, the LQG22 improves performance with elevation, following the same trend as a tuned integrator. These results are consistent with what was expected, as the diffraction-induced scintillation on the sensor is most critical at low elevations.

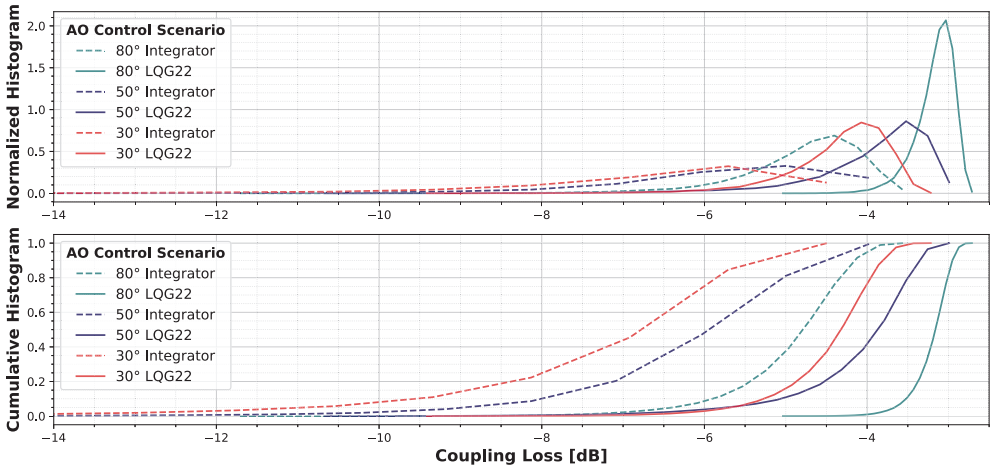

Fig. 5. Normalized histogram (top) and cumulative histogram (bottom) comparison of LQG22 with the integrator (benchmark) at the different simulated elevations. Each line style corresponds to a controller: dashed lines represent the integrator and solid lines represent LQG22. The colors represent the different elevations: red 30°; blue 50°, and teal 80°. The x-axis shows the coupling loss in decibel (dB), while the y-axes indicate the normalized histogram and the cumulative probability of the coupling loss distribution, respectively.

Optics EXPRESS

Table 6. Coupling loss and fading statistics for LQG22 on SimID50°, with SE±0.02 dB.

SimID50°	Coupling Loss (dB)		−3 dB		−6 dB		−10 dB	
	Mean	Med.	F/s	ms	F/s	ms	F/s	ms
Integrator	−5.69	−5.42	19	2.35	3	1.84	< 1	1.88
LQG22	−3.96	−3.73	6	2.39	< 1	0.63	0	–

Table 7. Coupling loss and fading statistics for LQG22 on SimID80° (SE±0.01dB).

SimID80°	Coupling Loss (dB)		−3 dB		−6 dB		−10 dB	
	Mean	Med.	F/s	ms	F/s	ms	F/s	ms
Integrator	−4.80	−4.64	3	1.76	< 1	1.00	0	–
LQG22	−3.17	−3.12	0	–	0	–	0	–

4.3. Performance robustness to elevation

In order to assess performance robustness of LQG controllers designed with turbulence profiles calculated for the wrong elevation, we have chosen to design an LQG22 controller in the SimID30° case, and to use this controller at other elevations. The following results were thus all obtained with erroneous priors corresponding to a 30° of elevation.

The curves on Fig. 6 show a visible performance degradation, most accentuated at 50° with regards to the optimal controller for each case shown in Fig. 5.

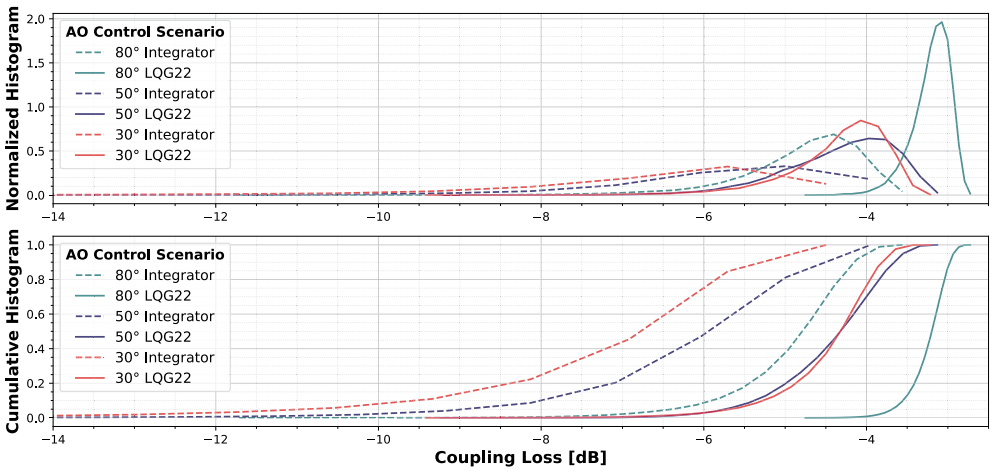

Fig. 6. Normalized histogram (top) and cumulative histogram (bottom) comparison of integrator and LQG22 keeping priors for SimID30° but simulated at different elevations (SimID50° and SimID80°).

The case where priors are taken using SimID50° and the LQG regulator is applied to the SimID30° scenario has also been tested, and the performance collapses. When the elevation of the LEO satellite decreases, resulting in higher wind velocities and lower r_0, decorrelation is faster. This aspect of temporal decorrelation in the model with respect to the true wind profile has been looked at in [26] in astronomical AO. With models based on wind velocities, it was found that using models with faster decorrelation than that induced by the true profile led to better results [26]. So we can anticipate that in FSOC, when the elevation of the LEO satellite decreases, model updates should be more frequent. If updates cannot be done frequently enough,

Optics EXPRESS

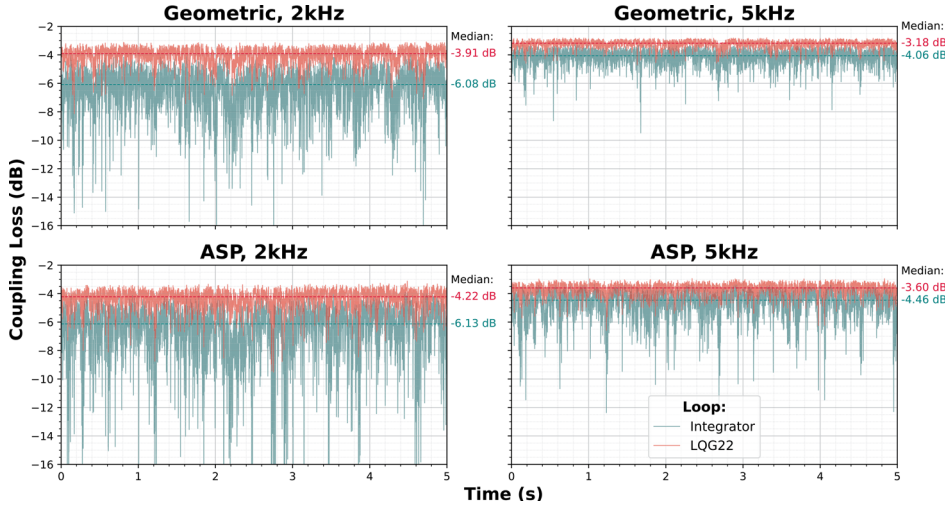

Fig. 7. Coupling loss comparison between a tuned integrator (teal) and LQG22 (red) for SimID30° at 2 and 5 kHz, with geometric and angular spectrum propagation methods.

the results of Fig. 6 suggest that priors should correspond to the worst case in order to limit performance loss. This of course deserves further investigation and experimental validations.

4.4. Impact of physical propagation on data rates

The interest in predictive control is a direct consequence of understanding the AO temporal error as a significant hindrance in the link budget that cannot otherwise be addressed. One could present the hypothesis that increasing the sampling rate could reduce the temporal error and mitigate the effects of scintillation. However, geometric propagation does not accurately represent scintillation and gives optimistic results. In order to quantify the difference, a comparison between geometric and physical propagation was made at 30° elevation, at both 2 and 5 kHz, with LQG and integrator controllers.

The results are shown in Fig. 7. Each plot represents 5 seconds of simulated data of the same time series (i.e. same initial phase screens) with different sampling and propagation methods, accordingly. The results highlight the effectiveness of the predictive regulator at mitigating the fades in all cases. Focusing solely on the geometric propagation cases at 2 and 5 kHz, the LQG at 2 kHz achieves similar median coupling loss as an integrator running at 5 kHz, in agreement with [11] where the authors compare behaviors at 2 and 4 kHz in geometric propagation only. However, when considering the full physical propagation effects, LQG median coupling at 2 kHz is still better than integrator at 5 kHz. In addition, the increase of severe deep fades is evidenced when taking into account the physical effects of scintillation.

The fade statistics at −3, −6 and −10 dB are shown in Table 8. These results support that LQG regulators are not only effective at improving median coupling efficiency but also at mitigating the fade count, depth and their duration. Furthermore, whilst running the loop at higher rates decreases the fade statistics, the plot of ASP at 5 kHz shows that integrator is still affected by scintillation, as opposed to the LQG with no reported drops below 50% of the power (i.e. −3 dB fades). This suggests that simply running the integrator at higher loop frequencies is not sufficient to obtain a stable link, and an LQG regulator provides a clear advantage regardless of loop rate. This is consistent with the hypothesis that a predictive controller such as the LQG can help mitigate the temporal error with effective prediction.

Optics EXPRESS

Table 8. Fade statistics at 2 kHz and 5 kHz for integrator and LQG controllers under geometric and ASP propagation.

		−3 dB		−6 dB		−10 dB	
Controller	**Propagation**	**F/s**	**Dur.**	**F/s**	**Dur.**	**F/s**	**Dur.**
2 kHz							
Integrator	Geometric	35	1.45	6	1.13	1	0.85
	ASP	42	1.86	15	1.33	4	1.08
LQG22	Geometric	1	1.26	0	–	0	–
	ASP	3	1.02	0	–	0	–
5 kHz							
Integrator	Geometric	1	0.73	0	–	0	–
	ASP	14	1.27	2	0.62	0	–
LQG22	Geometric	0	–	0	–	0	–
	ASP	0	–	0	–	0	–

The performance of the integrator at 5 kHz shown in Table 8 quantifies the impact of different propagation methods. Introducing the physical propagation (ASP) increases the mean fade duration from 0.73 to 1.27 ms. Considering bandwidths of the order of 10 Tbit/s [27], it could represent a mean data rate loss of about 12.7 Gbit/s. This loss goes unaccounted for if only geometric simulation is used.

Finally, Fig. 8 shows the performance of the different regulators at different loop rates for the scenarios in which physical propagation is used. Here it is further evidenced that whilst the increased loop rate leads to a significant performance increase with a tuned integrator, the LQG at

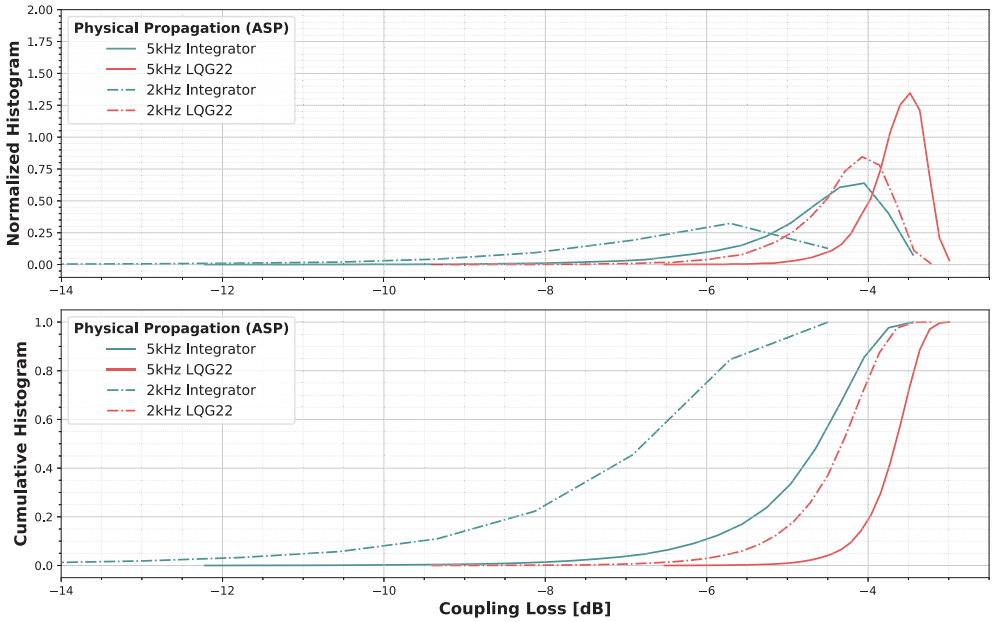

Fig. 8. Normalized histogram (top) and cumulative histogram (bottom) for physical propagation method controller comparison at 2 kHz (dash-dotted line) and 5 kHz (solid line), with the integrator performance drawn in teal, and LQG22 in red.

Optics EXPRESS

2 kHz still outperforms the integrator at 5 kHz, as highlighted above, due to the aforementioned ability to mitigate the fades as well as directly reduce the impact of the temporal error.

5. Moving towards on-sky demonstration

The results have shown that a zonal-based LQG with oversampling of the phase grid and edge compensation consistently outperforms the integrator in all scenarios studied in this paper. The robustness to fades and improved median coupling loss motivate the steps towards lab demonstration and on-sky implementation.

While lab conditions can be controlled, on-sky conditions change quickly. The LQG controllers here considered are based on time invariant parameters with an infinite horizon criterion (residual phase variance) enabling use of asymptotic Kalman gain without loss of optimality.

The natural atmospheric wind has not been accounted for in our simulations. However, accounting for it in the modeling is straightforward as this only modifies wind norms and directions. Because the apparent wind is dominant, performance variation induced by natural wind should be limited and not modify the conclusions. As a matter of fact, performance in terms of Strehl ratio is robust to errors on wind priors, as shown in [10] for the ground layer and in [28] with natural wind on 3 layers with weak and strong errors on apparent wind's norm and direction. Because coupling efficiency tends to follow the Strehl ratio, the benefit should be similar. As for wind profile estimation, the error bars considered in [28] are consistent with the resolution given by the Stereo-SCIDAR [29]. Of course the question of performance robustness to priors mismatch is of great interest in the framework of strong scintillation FSOC scenarios. To this day scintillation remains the subject of many studies due to the resulting measurement degradation observed with current wavefront sensing techniques and its detriment to AO loop stability [30–33]. Further investigation on mitigating its impact requires consideration of all the priors involved and would thus deserve additional and thorough studies which are out of the scope of this paper.

In practice evolving turbulent conditions require regular updates of the state model together with the associated fudge factor to ensure high performance. An autonomous LQG controller (with automatic controller updates) has been for example successfully validated on sky on GTC (Gran Telescopio Canarias) on the GTCAO system [34]. Note that this autonomous LQG regulator mixes models based on machine learning techniques and priors learned from telemetry data. This can be done easily in a state space framework, as we could for example mix the zonal model, efficient for frozen flow representation, and machine learning for the ground layer model, thus allowing to account for nonlinearities and complex disturbances that inevitably occur on real systems (i.e. vibrations, mount jitter). The update rate will need to be defined according to on-site conditions and to performance robustness to priors mismatch. It is thus difficult to anticipate here an appropriate value.

It is worth highlighting that LQG controllers based on asymptotic Kalman filters to control a full AO system have a proven track record of successful on-sky demonstrations in astronomy [24,35,36]. We are thus confident that they can be successful for FSOC on-sky operations. The main challenges should be faster evolution of observing conditions and strong scintillation. The latter could be addressed by using for example a non-asymptotic Kalman filter.

In LEO applications, elevation plays a crucial role in terms of AO control performance, as can be seen in Fig. 5 where results highlight a strong dependency with elevation for all regulators. As the elevation is lowered, so is the median coupling loss, and the fade count increases. However, we have shown that when taking the 30° case as prior for all elevation cases the LQG controller has systematically outperformed the integrator. For on-sky applications where elevation will evolve rapidly, this suggests frequent controller updates shouldn't be needed.

Optics EXPRESS

It is important to note that these periodical regulator updates may lead to transients in feedback loops. These control "bumps" could potentially be detrimental to performance, and mitigation techniques should therefore be considered, such as the anti-bump adapter reported in [37].

As for real-time computation, it is important to note that the critical path that goes from measurements to commands application has exactly the same complexity as the integrator whatever the state size [26]. Remaining calculations can then be done efficiently in idle time thanks to parallelization, all the more when the model is expressed in a zonal basis. Ultimately, a fully decoupled LQG regulator in the Fourier domain has been for example demonstrated on an AO bench at 8 kHz [38].

6. Conclusion

The focus of this work is on the use of predictive control on FSOC LEO links, specifically considering the requirements during daytime turbulence conditions at low elevations and taking into account the physical propagation effects through ASP. A zonal-based LQG regulator with theoretical priors formulated as in [10] is shown to outperform the integrator in all considered scenarios.

Potential LQG model improvements are explored, such as the effects of wavefront sensor measurement oversampling and edge compensation. Three different architectures are then compared to a standard integrator in an end-to-end Monte Carlo simulator with diffraction effects included at low elevation, with strong apparent wind and resulting dominating frozen flow effect. It was shown that all LQG architectures outperform a tuned integrator in terms of mean and median coupling loss, as well as the fade level statistics considered (3 dB, 6 dB, 10 dB). The best performance is mainly achieved by leveraging the phase oversampling, while edge compensation provides marginal improvement.

An LQG optimised for 30° elevation is then simulated for 50 and 80° elevations in order to depict a LEO link with the same regulator, and it outperforms the integrator. However, we have pointed out that when the LQG regulator is optimized for weaker turbulence and lower wind velocities (resulting in a model with slower decorrelation), performance may collapse. This suggests that regular updates are needed when observation conditions degrade, or that performance loss may be limited by using the most pessimistic priors.

When it comes to very low elevations (i.e. 10° to 20°), prediction may no longer lead to performance improvement as the temporal error may no longer be dominant. However we can expect the LQG AO loop to be more robust to the fast intensity fluctuations on the detector induced by the strong scintillation.

Including physical propagation effects in simulation leads to a significant fade count increase. This shows that the usual geometric propagation under represents the fade events by not accounting for scintillation. As a consequence, geometric simulation results were shown to be optimistic, especially at lower elevation. These results go hand-in-hand with theoretical expectations [19].

Increasing the loop frequency to 5 kHz improves performance for all regulators. However, the LQG considerably increases the median coupling and lowers fade counts, without any fade below −3 dB, which demonstrates a robustness vital for FSOC-AO. Furthermore, the LQG regulator at 2 kHz outperforms the integrator controller at 5 kHz, showing that simply increasing the loop rate is not sufficient to counteract the effect of scintillation. These results are consistent with long standing reports in astronomy AO that deploying an LQG improves the performance, bypassing the need to increase the loop rate [39]. This has more recently been confirmed to also be the case for coupling efficiency in geometric propagation simulations [11].

The LQG led to the most significant increase in performance at a 30° elevation with respect to the integrator. In that configuration, the mean coupling loss is improved by 2.3±0.02 dB, and the coupling efficiency by 70%. The 3 dB fades are reduced by 93%, and their mean duration shortened by about 45%, whilst the deeper fade levels are fully mitigated.

Optics EXPRESS

These results warrant further investigation and particularly experimental demonstrations. These could ideally be achieved initially in a controlled lab environment, which would constitute a natural extension of the work hereby presented and establish a stepping stone into on-sky link testing with LEO satellites in a near future.

Funding. Deutscher Akademischer Austauschdienst (57540125).

Acknowledgements. The authors wish to thank Janis Surof, Samuele Raffa, Dr. Lisa Bardou and Prof. James Osborn for the numerous fruitful discussions. The atmospheric profiles are adapted from Project HydRON-DS Phase A/B1, ESA Contract No. 4000136544/21/NL/CLP. The results presented in this paper make use of Python and libraries such as NumPy, Matplotlib, Pandas and AOTools.

Disclosures. The authors declare no conflicts of interest.

Data Availability. Data underlying the results presented in this paper are not publicly available at this time but may be obtained from the authors upon reasonable request.

References

1. A. Jahid, M. H. Alsharif, and T. J. Hall, "A contemporary survey on free space optical communication: Potentials, technical challenges, recent advances and research direction," J. Network Computer Appl. **200**, 103311 (2022).
2. Space Agency European, "ESA Specification for Terabit/sec Optical Links (ESTOL)," Tech. rep., ESA Public Report (2023).
3. G. Acar, D. Arapoglou, E. Re, *et al.*, "HydRON Vision: preparation towards a flight demonstration," in *International Conference on Space Optics-ICSO 2022*, vol. 12777 (SPIE, 2023), pp. 1656–1673.
4. L. C. Andrews and R. L. Phillips, *Laser beam propagation through random media, Second Edition* (SPIE digital library, 2005).
5. R. K. Tyson and B. W. Frazier, *Principles of adaptive optics* (CRC press, 2022).
6. R. M. Calvo, J. Poliak, J. Surof, *et al.*, "Optical technologies for very high throughput satellite communications," in *Free-Space Laser Communications XXXI*, vol. 10910 (SPIE, 2019), pp. 189–204.
7. J. Torres, A. Reeves, C. Kulcsár, *et al.*, "Turbulence Characterization of a Free Space Optical Communication Link for High Performance Adaptive Optics Control," in *Adaptive Optics and Applications*, (Optica Publishing Group, 2022), pp. OF2B–2.
8. H. F. Kelemu, A. Reeves, R. M. Calvo, *et al.*, "Investigation of advanced control for adaptive optics in free-space optical communication," in *Environmental Effects on Light Propagation and Adaptive Systems V*, vol. 12266 (SPIE, 2022), pp. 51–60.
9. C. A. Primmerman, T. R. Price, R. A. Humphreys, *et al.*, "Atmospheric-compensation experiments in strong-scintillation conditions," Appl. Opt. **34**(12), 2081–2088 (1995).
10. L. Prengère, C. Kulcsár, and H.-F. Raynaud, "Zonal-based high-performance control in adaptive optics systems with application to astronomy and satellite tracking," J. Opt. Soc. Am. A **37**(7), 1083–1099 (2020).
11. P. Robles, C. Petit, J.-M. Conan, *et al.*, "Predictive adaptive optics for satellite tracking applications: optical communications and satellite observation," in *Adaptive Optics Systems VIII*, vol. 12185 (SPIE, 2022), pp. 917–931.
12. I. R. Hristovski, J. Osborn, O. J. Farley, *et al.*, "Pre-distortion adaptive optics for optical feeder links: simulations and performance analyses," Opt. Express **32**(12), 20976–20991 (2024).
13. L. C. Andrews and R. L. Phillips, *Laser Beam Propagation through Random Media* (SPIE Press, 2005), 2nd ed.
14. G. L. Torre, S. Raffa, J. Poliak, *et al.*, "A spectral shaping approach to generate power vectors for optical ground-to-space links," in *Proc. SPIE 13194, Environmental Effects on Light Propagation and Adaptive Systems VII*, (2024), p. 131940N.
15. T. Fusco, J.-M. Conan, V. Michau, *et al.*, "Efficient phase estimation for large-field-of-view adaptive optics," Opt. Lett. **24**(21), 1472–1474 (1999).
16. D. P. Greenwood, "Bandwidth specification for adaptive optics systems," JOSA **67**(3), 390–393 (1977).
17. L. F. Beesley, R. Griffiths, K. Hartley, *et al.*, "Demonstration of 24-hour continuous optical turbulence monitoring in a city," Opt. Express **33**(5), 10140–10149 (2025).
18. J. Schmidt, *Numerical Simulation of Optical Wave Propagation with Examples in MATLAB*, Press monograph (SPIE, 2010).
19. D. L. Fried and J. L. Vaughn, "Branch cuts in the phase function," Appl. Opt. **31**(15), 2865–2882 (1992).
20. B. L. Roux, J.-M. Conan, C. Kulcsár, *et al.*, "Optimal control law for classical and multiconjugate adaptive optics," J. Opt. Soc. Am. A **21**(7), 1261–1276 (2004).
21. D. P. Looze, "Linear-quadratic-Gaussian control for adaptive optics systems using a hybrid model," J. Opt. Soc. Am. A **26**(1), 1–9 (2009).
22. C. Kulcsár, H.-F. Raynaud, C. Petit, *et al.*, "Minimum variance prediction and control for adaptive optics," Automatica **48**(9), 1939–1954 (2012).
23. C. Petit, J.-M. Conan, C. Kulcsár, *et al.*, "Linear Quadratic Gaussian control for adaptive optics and multiconjugate adaptive optics: experimental and numerical analysis," J. Opt. Soc. Am. A **26**(6), 1307–1325 (2009).

Optics EXPRESS

24. B. Sinquin, L. Prengère, C. Kulcsár, *et al.*, "On-sky results for adaptive optics control with data-driven models on low-order modes," Mon. Not. R. Astron. Soc. **498**(3), 3228–3240 (2020).
25. F. Roddier, *Adaptive optics in astronomy* (Cambridge university press, 1999).
26. L. Marquis, "High-performance adaptive optics control for the Gran Telescopio Canarias," Ph.D. thesis, Université Paris-Saclay; Universidad de La Laguna (2023).
27. A. Dochhan, J. Poliak, J. Surof, *et al.*, "13.16 Tbit/s Free-space Optical Transmission over 10.45 km for Geostationary Satellite Feeder-links," in *Photonic Networks; 20th ITG-Symposium*, (2019), pp. 1–3.
28. L. Prengère, C. Kulcsár, and H.-F. Raynaud, "Predictive controllers for high dynamic atmospheric turbulence compensation. Application to Low-Earth Orbit satellite tracking," in *OPTRO 2020 – International Conference on Electro-Optical Remote Sensing*, (Paris, France, 2020).
29. J. Osborn, T. Butterley, M. J. Townson, *et al.*, "Turbulence velocity profiling for high sensitivity and vertical-resolution atmospheric characterisation with Stereo-SCIDAR," Mon. Not. R. Astron. Soc. **464**(4), 3998–4007 (2016).
30. D. R. Gerwe, J. P. Stone, and H. B. Schall, "Closed-loop control for adaptive optics wavefront compensation in highly scintillated conditions," in *Laser Systems Technology*, vol. 5087 (SPIE, 2003), pp. 87–102.
31. D. Lechner, A. Zepp, M. Eichhorn, *et al.*, "Adaptable Shack-Hartmann wavefront sensor with diffractive lenslet arrays to mitigate the effects of scintillation," Opt. Express **28**(24), 36188–36205 (2020).
32. T. Vène, A. Bonnefois, J.-M. Conan, *et al.*, "Revisiting Shack-Hartmann wavefront sensor design for space-ground communications in strong scintillation conditions," in *Adaptive Optics for Extremely Large Telescopes 7th Edition* (2023).
33. T. Vène, A. Bonnefois-Montmerle, L. M. Mugnier, *et al.*, "LEO-to-ground low elevation optical communication: optimization of an adaptive optics design robust to scintillation," in *Free-Space Laser Communications XXXVII*, vol. 13355 (SPIE, 2025), pp. 367–372.
34. N. Galland, L. Marquis, H.-F. Raynaud, *et al.*, "Autonomous predictive control for the Gran Telescopio Canarias Adaptive Optics (GTCAO) system within the H2020 ORP project: progress and initial results," in *Adaptive Optics Systems IX*, vol. 13097 (SPIE, 2024), pp. 1908–1914.
35. G. Sivo, C. Kulcsár, J.-M. Conan, *et al.*, "First on-sky SCAO validation of full LQG control with vibration mitigation on the CANARY pathfinder," Opt. Express **22**(19), 23565–23591 (2014).
36. L. Marquis, H.-F. Raynaud, N. Galland, *et al.*, "First on-sky tests of LQG control for a 10m-class telescope: prelude on the Gran Telescopio Canarias adaptive optics system," in *Adaptive Optics Systems IX*, vol. 13097 (SPIE, 2024), pp. 1869–1875.
37. H.-F. Raynaud and C. Kulcsár, "Controller switching with the anti-bump adapter," Eur. J. Control. **80**, 101116 (2024).
38. L. A. Poyneer, S. M. Ammons, M. K. Kim, *et al.*, "Laboratory demonstration of the prediction of wind-blown turbulence by adaptive optics at 8 kHz with use of LQG control," Appl. Opt. **62**(8), 1871–1885 (2023).
39. J.-M. Conan, H.-F. Raynaud, C. Kulcsár, *et al.*, "Are integral controllers adapted to the new era of ELT adaptive optics?" in *AO4ELT2* (2011).